

# Field-Aligned Isotropic Surface Remeshing

Xingyi Du<sup>1,\*</sup>, Xiaohan Liu<sup>2,3,\*</sup>, Dong-Ming Yan<sup>2,3</sup>, Caigui Jiang<sup>4</sup>, Juntao Ye<sup>2,3</sup> and Hui Zhang<sup>1,†</sup>

<sup>1</sup>Software School, Tsinghua University, China

du-xy15@mails.tsinghua.edu.cn, huizhang@tsinghua.edu.cn

<sup>2</sup>NLPR, Institute of Automation, Chinese Academy of Sciences, China

liuxiaohan2017@ia.ac.cn, yandongming@gmail.com, juntao.ye@ia.ac.cn

<sup>3</sup>University of Chinese Academy of Sciences, China

<sup>4</sup>Max Planck Institute for Informatics, Germany

caigui.jiang@mpi-inf.mpg.de

## Abstract

We present a novel isotropic surface remeshing algorithm that automatically aligns the mesh edges with an underlying directional field. The alignment is achieved by minimizing an energy function that combines both centroidal Voronoi tessellation (CVT) and the penalty enforced by a six-way rotational symmetry field. The CVT term ensures uniform distribution of the vertices and high remeshing quality, and the field constraint enforces the directional alignment of the edges. Experimental results show that the proposed approach has the advantages of isotropic and field-aligned remeshing. Our algorithm is superior to the representative state-of-the-art approaches in various aspects.

**Keywords:** digital geometry processing, modelling, mesh generation

**ACM CCS:** I.3.6 [Computer Graphics]: Methodology and Techniques—Remeshing

## 1. Introduction

Triangle meshes are commonly used in computer graphics and other applications. Nowadays, meshes can be acquired with high accuracy using multiple methods, for example, using three-dimensional (3D) laser scanners, RGBD cameras, dense reconstruction from multi-view stereo images and isosurface contouring. Using these acquired raw meshes directly in downstream applications is difficult because they usually contain redundant data and have poor mesh quality. Remeshing is necessary to improve mesh quality while preserving the original geometry.

Various application-oriented criteria for surface remeshing are available. In this work, we focus on the widely used isotropic remeshing. Three common criteria should be followed by remeshing algorithms: simplicity, low approximation error and high mesh quality [AUGA08]. However, these goals usually conflict with one another, for example, highly regular meshes might have more distorted triangles than irregular meshes, whereas meshes with high triangle quality always contain more singular vertices, for example, remeshing with *Centroidal Voronoi Tessellation* (CVT) [DFG99]. Figure 1 illustrates this fact.

\*Both are joint first authors.

†Correspond author.

Directional fields can be naturally defined on surfaces and are commonly used for quadrilateral remeshing. Typical directional fields include principal curvature directions [BLP\*13], conjugate direction fields [LWX\*11] and harmonic fields [DKG05]. The edges of quad meshes are naturally aligned with the underlying fields via global parameterization. However, field alignment in isotropic remeshing is rarely considered. The lack of field-alignment causes ‘twisting’ artefacts near cylindrical regions and surface features, as illustrated in Figure 4 of [NPPZ11]. Even in isotropic regions, the lack of global alignment leads to local orientation conflict between neighbouring areas, and consequently produces unnecessary singular vertices, that is, possession of valences other than 6, as shown in Figure 1. The recent work of Jakob *et al.* [JTPS15] proposed an algorithm called *Instant Field-aligned Meshing* (IFM) for generating isotropic triangle meshes that simultaneously align to a predefined underlying directional field. Although highly regular triangle meshes with only a few singular vertices are generated, triangle quality is sacrificed due to distortion.

In this work, we propose a novel approach for field-aligned isotropic remeshing. We use six-way rotational symmetry (6-RoSy) fields to represent the target orientation of the output mesh edges because 6-RoSy fields are the most natural guidance fields for triangle meshes. However, our formulation can be generalized to other



**Figure 1:** Comparison of our approach with representative state-of-the-art approaches; from left to right: 6-RoSy field defining on the Moai surface, remeshing results of blue-noise sampling [YW13], discrete mesh optimization [DVBB13], centroidal Voronoi tessellation [YLL\*09], instant field-aligned meshing [JTPS15] and our result. The irregular vertices of the remeshes are coloured blue (degree < 6) and pink (degree > 6). The mesh quality is given in Table 2. Our remeshing is isotropic and field-aligned; that is, it has a few irregular vertices similar to [JTPS15] while keeping the mesh quality as good as in a CVT-based method [YLL\*09].

fields. Our method is built upon a remeshing framework that is based on CVT and the *restricted Voronoi diagram* (RVD) on surfaces [YLL\*09]. We add a novel penalty term to the CVT energy function to enforce the mesh edges to align with the underlying field. The presented approach, called Field-aligned CVT (FCVT), preserves the advantages of CVT, and the directional features of the field. Furthermore, we incorporate valence optimization operations in our remeshing framework to improve mesh quality. The main contributions of this paper are the following:

- A novel formulation for field-aligned isotropic remeshing.
- A simple interpolation method for 6-RoSy fields.
- A comprehensive comparison of proposed method with recent representative state-of-the-art approaches.

## 2. Related Works

Isotropic surface remeshing has been extensively studied. Representative approaches include particle reactions [Tur92, MKW07, BLW10, AGY\*17], Delaunay insertion [Che93, Boi05, CDS12], discrete local operators [HDD\*93, BK04, AYZ12, DVBB13, HYB\*17], randomized sampling [YW13, GYJZ15, ERA\*16] and variational approaches, for example, *centroidal Voronoi tessellation* (CVT) [DFG99], *optimal Delaunay triangulation* (ODT) [Che04] and their variations [FAKG10, CCW12, Ren16]. CVT-based approaches gain considerable attention due to their elegant theoretical background and the capability to generate high-quality meshes. These approaches can further be classified into several categories according to how the Voronoi diagram on surfaces are computed, for example, mesh parameterization [AMD02, AVDI03, SAG03], discrete clustering [VCP08, LWH\*15], RVD [YLL\*09, YBZW14, YW16] and geodesic Voronoi diagram [SSG03, FZ08,

WYL\*15, LXY\*16]. Additional details about the recent advantages of surface remeshing are available in the comprehensive survey by Alliez *et al.* [AUGA08] and the textbook by Botsch *et al.* [BKP\*10].

Although these isotropic algorithms generate high-quality meshes efficiently, they cannot produce good results near highly non-isotropic regions, for example, the cylindrical bending areas of CAD models. Anisotropic remeshing algorithms aim to handle such cases, but tend to introduce many thin and long triangles [LB12, ZGW\*13, FLSG14, BSTY15], thereby limiting their use in regular pattern synthesis [NPPZ11], where isotropic elements are preferred.

A natural way to align mesh edges with the principal direction involves defining a directional field on the input domain and then extracting the new mesh from the field with respect to a user-specified precision. The most well-known directional field is the min/max principal curvature directions, which is commonly used for quadrilateral remeshing [BLP\*13] or quad-dominant mixed remeshing [ACSD\*03, LL10].

Isotropic triangle meshes can be extracted from 6-RoSy directional fields through several approaches. For example, Lai *et al.* [LJX\*10] proposed a method of generating 6-RoSy fields that allow users to fully control and interactively modify the field topology. Huang *et al.* [HZP\*11] used 6-RoSy and density fields to generate three scalar fields on the input surface and construct meshes by extracting the isolines of the scalar fields. Nieser *et al.* [NPPZ11] used 6-RoSy field-guided global parameterization to generate triangular and hexagonal meshes. The field is aligned to one of the principal directions, which is automatically selected by the algorithm. However, long and thin triangles produced by parameterization distortion still exist. Jakob *et al.* [JTPS15] proposed the extrinsic smooth directional field, which aligns better to features than the

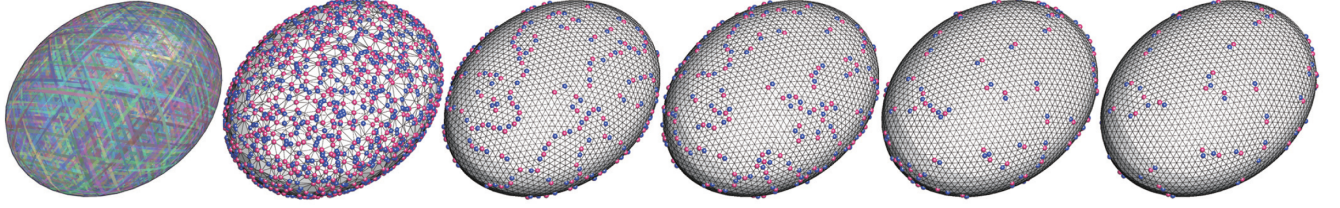


**Figure 2:** From left to right are: the field, initial mesh, result of CVT, result of 10 iterations, 50 iterations and final result.

previous ‘intrinsic smooth’ fields. Nevertheless, the mesh quality of this approach still suffers from distortion caused by tracing the field.

### 3. Field-Aligned CVT Formulation

In this work, we propose a novel field-aligned isotropic remeshing algorithm, that is based on CVT and field remeshing techniques. Field alignment is enforced by a penalty term added to the CVT energy. Given an input mesh surface  $\mathcal{M}$  and a set of sampled points  $\mathbf{X}$  on  $\mathcal{M}$ , we propose the following energy function:

$$E_{\text{tot}} = E_{\text{CVT}} + \lambda E_{\text{field}},$$

where  $\lambda \geq 0$  is a user-specified parameter, which balances the relative importance of the directional alignment requirement. In the rest of this section, we first introduce the basic concepts of CVT, RoSy fields and the extrinsic smoothness of a given field, and then discuss the details of the proposed field alignment term. The typical pipeline of our remeshing algorithm includes vector field generation, random initial sampling, CVT optimization and field-aligned CVT optimization, as illustrated in Figure 2. We give the prerequisite definitions and explain each step in the following.

#### 3.1. Centroidal Voronoi tessellation

The CVT energy term is defined as

$$E_{\text{CVT}}(\mathbf{X}) = \sum_{i=1}^n \int_{\Omega_i \cap \mathcal{M}} \rho(\mathbf{x}) \|\mathbf{x} - \mathbf{x}_i\|^2 d\sigma, \quad (1)$$

where  $\Omega_i \cap \mathcal{M}$  is the *restricted Voronoi cell* (RVC) [YLL\*09] of the point  $\mathbf{x}_i$  defined as the intersection of the Voronoi cell  $\Omega_i$  of  $\mathbf{x}_i$  and the mesh surface  $\mathcal{M}$ ;  $\rho(\mathbf{x}) > 0$  is a user-defined density function. When  $\rho$  is constant, a uniform CVT is obtained. The dual nature of the RVD as a remeshing of  $\mathcal{M}$  is called *restricted Delaunay triangulation* (RDT).

#### 3.2. Rotational symmetry field

The RoSy field is commonly used in parameterization and quadrilateral mesh generation.  $N$ -way rotational symmetry ( $N$ -RoSy) field over a surface defines  $N$  distinct directions at every surface point  $\mathbf{x}$ , where all the directions lie in the tangent plane at  $\mathbf{x}$  and each pair of adjacent directions form an angle of  $\frac{2\pi}{N}$ . Here, a 6-RoSy field is used as the target orientation for mesh edges because it naturally implies

the symmetry of regular triangular mesh. Additional details about the directional field are available in recent survey papers [dGDT16, Zha16, VCD\*16].

#### 3.3. Extrinsic smoothness property

The extrinsic smoothness proposed in [JTPS15] measures the smoothness of a given RoSy field by calculating the difference between proximate field directions directly in 3D space. Jakob *et al.* [JTPS15] experimentally demonstrated that extrinsic smoothness leads to an improved alignment to the sharp features of the input surface. A theoretical analysis of extrinsic smoothness was also provided by Huang and Ju [HJ16].

Similar to field smoothing, our field alignment solution aims to minimize the difference between the edge direction and the direction of the local field. Inspired by the extrinsic smoothness, we measure the difference directly in 3D space, thus simply yet powerfully formulating the field alignment constraint.

#### 3.4. Field alignment

The field alignment term is formulated as the weighted sum of the directional distance  $D$  of all mesh edges in RDT of  $\mathbf{X}$  on  $\mathcal{M}$ .

$$E_{\text{field}}(\mathbf{X}) = \sum_{i=1}^n \sum_{j \in \mathcal{N}(i)} w_{ij} \cdot D_{ij}, \quad (2)$$

where  $\mathcal{N}(i)$  denotes the neighbour points of  $\mathbf{x}_i$  and  $w_{ij}$  is the weight of edge  $e_{ij}$ .

A detailed derivation of the direction distance  $D$  is provided, and its properties in the case of 6-RoSy field is discussed. Given a sample point  $\mathbf{x}_i$  and its neighbour point  $\mathbf{x}_j$ ,  $e_{ij} = \mathbf{x}_j - \mathbf{x}_i$  is the direction vector of the edge between  $\mathbf{x}_i$  and  $\mathbf{x}_j$ ,  $\mathbf{n}_i$  is the unit normal vector and  $\mathbf{d}_i$  is the unit vector representing the  $N$ -RoSy field, that is, one of the  $N$  field vectors at  $\mathbf{x}_i$ .

Given  $\mathbf{n}_i$  and  $\mathbf{d}_i$ , a local coordinate system is established by a tuple of standard unit vectors  $\{\mathbf{d}_i, \mathbf{n}_i \times \mathbf{d}_i, \mathbf{n}_i\}$ . The directional angles  $\theta$  and  $\varphi$  of edge  $e_{ij}$  is then defined through a method common in spherical systems, as shown in Figure 3 (middle). The direction similarity of edge  $e_{ij}$  and local field  $\mathbf{d}_i$  can simply be measured by their inner product:

$$\begin{aligned} \mathbf{d}_i^T \left( \frac{\mathbf{e}_{ij}}{\|\mathbf{e}_{ij}\|} \right) &= (1, 0, 0) \cdot (\sin \theta \cos \varphi, \sin \theta \sin \varphi, \cos \theta)^T \\ &= \sin \theta \cos \varphi. \end{aligned}$$

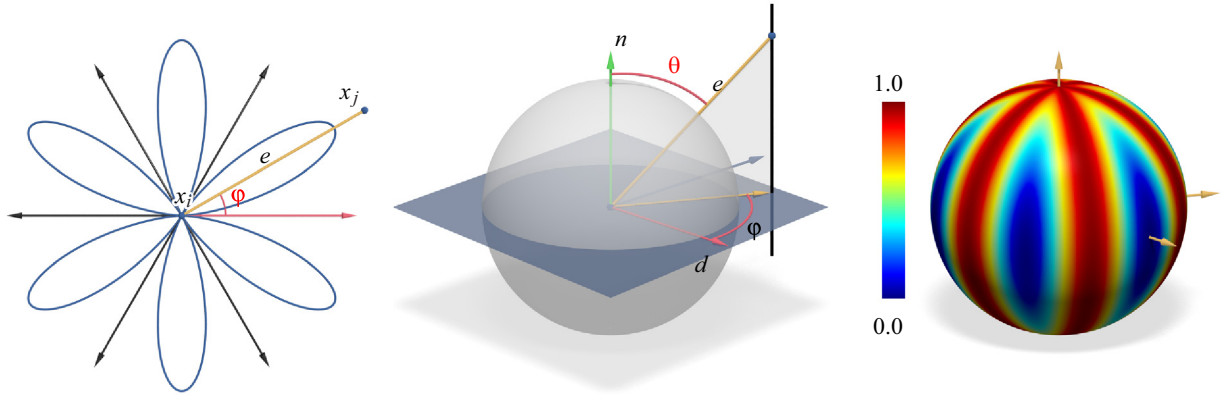


**Figure 3:** Left: 6-RoSy direction distance in 2D plane; middle: local coordinate system formed with local unit normal  $\mathbf{n}$  and the representing field vector  $\mathbf{d}$  at sample point; direction angles of edge  $e$  defined in local coordinate system; right: visualized 6-RoSy direction distance  $D_6$  on unit sphere; distance penalizes deviation from local field and restricts edges on the tangent plane.

To accord with the symmetry of the  $N$ -RoSy field,  $\varphi$  is multiplied with the symmetry number  $N$ , thereby giving the  $N$ -RoSy direction similarity  $S$ ,

$$S(\mathbf{e}_{ij}, \mathbf{n}_i, \mathbf{d}_i) = \sin \theta \cos(N\varphi).$$

$S$  is a  $\frac{2\pi}{N}$  period function of  $\varphi$  and thus not affected by the choice of  $d_i$ . To obtain the  $N$ -RoSy direction distance, we first map  $\cos(N\varphi)$  linearly to  $[0, 1]$ , which simultaneously maps  $S$  to  $[0, 1]$ . Then, we calculate the difference between 1 and the image of  $S$ . The  $N$ -RoSy direction distance  $D$  is

$$D(\mathbf{e}_{ij}, \mathbf{n}_i, \mathbf{d}_i) = 1 - \left( \frac{1 + \cos(N\varphi)}{2} \right) \sin \theta, \quad D \in [0, 1]. \quad (3)$$

To obtain an intuition of the field alignment term, we explore the 6-RoSy direction distance,

$$D_6 = 1 - \left( \frac{1 + \cos 6\varphi}{2} \right) \sin \theta.$$

Figure 3 (right) visualizes  $D_6$  on the surface of a unit sphere. Direction distance penalizes deviation from the local field and correctly represents the rotational symmetry. Figure 3 (left) illustrates  $D_6$  on the equatorial plane ( $\theta = \frac{\pi}{2}$ ). The direction distance is 0 when the edge coincides with one of the field directions and increases when the edge deviates from the field. Furthermore, distance restricts mesh edges to be on the local tangent plane because  $D_6$  will increase if  $\theta$  deviates from  $\frac{\pi}{2}$ .

### 3.5. Edge weight

The edge weight is used to ameliorate the smoothness of our field alignment term. Selecting a proper weight for each edge when edge flips are considered is shown in Figure 4. With a constant edge weight (e.g.  $w = 1$ ), the total energy changes abruptly during the edge flip, thereby making optimization difficult. To make the energy smooth, we assign small weights to flipping-prone edges. In Delaunay triangulation, an edge flips when two incident triangles share

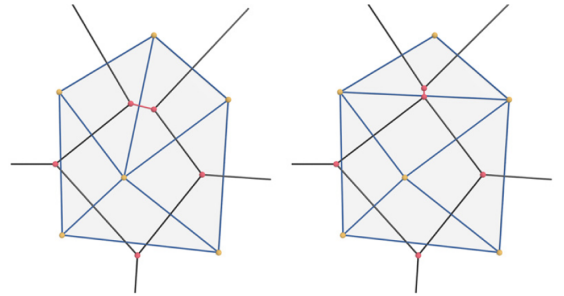


**Figure 4:** Delaunay triangulation and its dual Voronoi diagram when an edge flips.

a common circumscribed circle. Viewed from the dual perspective, the corresponding Voronoi edge disappears when the primal triangle edge flips. Thus, the field direction must be interpolated over the entire mesh surface.

## 4. Implementation Details

In this section, we present the implementation details of our field-aligned isotropic remeshing framework. The main building blocks are field initialization, interpolation and energy minimization.

### 4.1. Direction field initialization

We use the direction field generation proposed in [JTP15], which uses a mesh  $\mathcal{M}$  as input and outputs the normal and field directions for each vertex of  $\mathcal{M}$ . Normal and field directions are represented by unit 3D vectors. For triangle remeshing, a 6-RoSy field is used.

### 4.2. Direction field interpolation

To calculate the field alignment energy term for each sample point, the normal and field directions at the point are required.

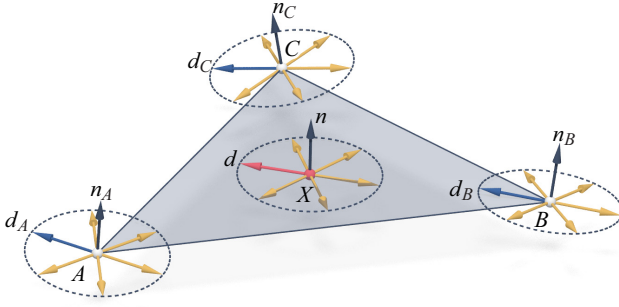


**Figure 5:** Normal and field direction interpolation in  $\triangle ABC$ .

However, the generated field is only defined on the vertices of the input mesh. Thus, the field direction over the entire mesh surface must be interpolated.

Direction interpolation over surface is a hard problem, especially for an  $N$ -RoSy field. For a 6-RoSy field, any of the six direction vectors can be chosen to represent the field direction at each vertex. Therefore, the interpolation method requires that the output direction is not affected by the choice of field representation. Besides, a smooth interpolation is desired to facilitate energy optimization, and this interpolation is not addressed in [JTPS15].

Here, we propose a novel interpolation scheme that interpolates normal and field directions over the mesh surface. We follow the piecewise paradigm to allow the interpolation result in a mesh triangle to be determined by the direction information at its three vertices.

Figure 5 shows the interpolation at point  $X$  in  $\triangle ABC$ . First, the normal direction is calculated as a weighted average of the normal directions of the three vertices:

$$\mathbf{n} = w_A \mathbf{n}_A + w_B \mathbf{n}_B + w_C \mathbf{n}_C.$$

Here, we use the well-known discrete harmonic weights, as suggested in [HJ16]. Then, we normalize the normal direction to unit length. Given the normal direction  $\mathbf{n}$ , the field direction is restricted to be orthogonal to  $\mathbf{n}$ . The direction  $\mathbf{d}$  that has the least angle deviation from the field directions at the three vertices is then found. Formally,  $\mathbf{d}$  is determined as the maximizer of the following energy:

$$\begin{aligned} E_{\text{interpolation}} &= w_A \mathbf{d}_A^T \mathbf{d} + w_B \mathbf{d}_B^T \mathbf{d} + w_C \mathbf{d}_C^T \mathbf{d} \\ &= (w_A \mathbf{d}_A + w_B \mathbf{d}_B + w_C \mathbf{d}_C)^T \mathbf{d} \\ &= \mathbf{d}_w^T \mathbf{d}, \end{aligned}$$

where  $\mathbf{d}_w$  denotes the weighted average of the field directions, which can be decomposed into two components: one orthogonal and another parallel to the normal vector  $\mathbf{n}$ :

$$\mathbf{d}_w = \mathbf{n} \mathbf{n}^T \mathbf{d}_w + (I - \mathbf{n} \mathbf{n}^T) \mathbf{d}_w.$$

Thus, the energy becomes

$$\begin{aligned} E_{\text{interpolation}} &= \mathbf{d}_w^T \mathbf{d} \\ &= \mathbf{d}_w^T \mathbf{n} \mathbf{n}^T \mathbf{d} + \mathbf{d}_w^T (I - \mathbf{n} \mathbf{n}^T) \mathbf{d} \\ &= \mathbf{d}_w^T (I - \mathbf{n} \mathbf{n}^T) \mathbf{d}. \end{aligned}$$

The energy is maximized when  $\mathbf{d}$  has the same direction as  $(I - \mathbf{n} \mathbf{n}^T) \mathbf{d}_w$ , and the maximal energy is  $\|(I - \mathbf{n} \mathbf{n}^T) \mathbf{d}_w\|$ . To eliminate the influence of the choice of representative vectors at the three vertices, we traverse all combinations of these vectors to find the combination that maximizes  $\|(I - \mathbf{n} \mathbf{n}^T) \mathbf{d}_w\|$ , thus also optimizing energy  $E_{\text{interpolation}}$ . Meanwhile, interpolated field direction  $\mathbf{d}$  is set to be length-normalized  $(I - \mathbf{n} \mathbf{n}^T) \mathbf{d}_w$ , which is produced by this combination of representation vectors.

Our method shares the concept of extrinsic field smoothness used in [HJ16] such that the difference between two directions is measured directly in 3D space. The result of interpolation is not affected by the choice of representative vectors. With a proper choice of weight, the smoothness is also guaranteed. Our interpolation method is simple and can be generalized to any arbitrary  $N$ -RoSy field.

#### 4.3. Energy minimization

We use a quasi-Newton solver (e.g. L-BFGS [LWL\*09]) to minimize the proposed energy function, where the functional gradient with respect to points  $\mathbf{X}$  is required. The gradient is composed of two parts  $E_{\text{CVT}}$  and  $E_{\text{field}}$ .

$$\frac{\partial E_{\text{tot}}}{\partial \mathbf{X}} = \frac{\partial E_{\text{CVT}}}{\partial \mathbf{X}} + \lambda \frac{\partial E_{\text{field}}}{\partial \mathbf{X}}.$$

Here,  $\frac{\partial E_{\text{CVT}}}{\partial \mathbf{x}_i} = 2m_i(\mathbf{x}_i - \mathbf{x}_i^*)$  [DFG99], where  $m_i$  is the mass of the RVC  $\Omega_{i|\mathcal{M}}$  and  $\mathbf{x}_i^*$  is the restricted centroid [YLL\*09].

For  $E_{\text{field}}$ , the partial derivative with respect to a sample point  $\mathbf{x}_i$  is

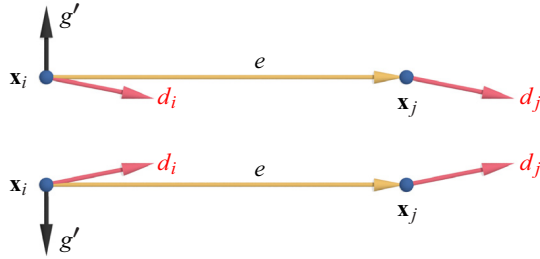
$$\frac{\partial E_{\text{field}}}{\partial \mathbf{x}_i} = \sum_{j \in \mathcal{N}(i)} \left( w_{ij} \cdot \frac{\partial D_{ij}}{\partial \mathbf{x}_i} + w_{ji} \cdot \frac{\partial D_{ji}}{\partial \mathbf{x}_i} \right),$$

where  $\mathcal{N}(i)$  denotes the neighbours of  $\mathbf{x}_i$ ,  $w_{ij}$  and  $w_{ji}$  are edge weights and  $D$  is the direction distance function. The detailed calculation of the gradient of  $D$  is given in the Appendix.

To demonstrate the effectiveness of our field alignment term, we analyse the energy gradient through a simple case of a 6-RoSy field in 2D plane, where  $\theta$  is always  $\pi/2$ . In the following discussion, we assume a Cartesian coordinate system with standard unit vectors  $\{\mathbf{e}_x, \mathbf{e}_y, \mathbf{e}_z\}$ , in which  $\mathbf{e}_x$  and  $\mathbf{e}_y$  lie in the 2D plane, and  $\mathbf{e}_z$  is the normal direction. The partial derivative of the field alignment term of edge  $e$  with respect to  $\mathbf{x}_i$  is

$$\frac{\partial E_e}{\partial \mathbf{x}_i} = 3(\sin 6(\varphi_e - \delta_i) + \sin 6(\varphi_e - \delta_j)) \cdot \frac{\mathbf{e} \times \mathbf{e}_z}{\|\mathbf{e}\|^2},$$

where  $\varphi_e$  is the directional angle of edge  $e$ ;  $\delta_i$  and  $\delta_j$  are the angles of field direction at  $\mathbf{x}_i$  and  $\mathbf{x}_j$ , respectively. These angles are relative to  $\mathbf{e}_x$ .



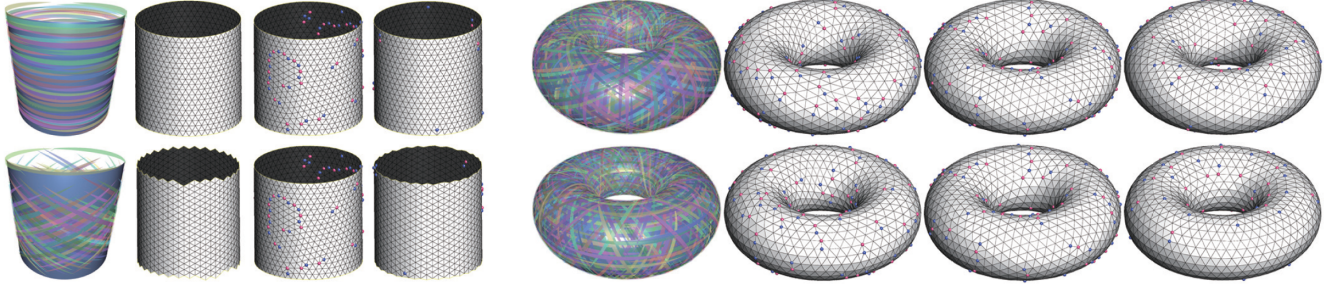
**Figure 6:** Opposite gradient directions of field alignment energy in two different constant fields.

Figure 6 shows an edge in two different constant fields. In both cases, the opposite gradient direction  $g'$  is the right moving direction for  $\mathbf{x}_i$  to align the edge with the field.

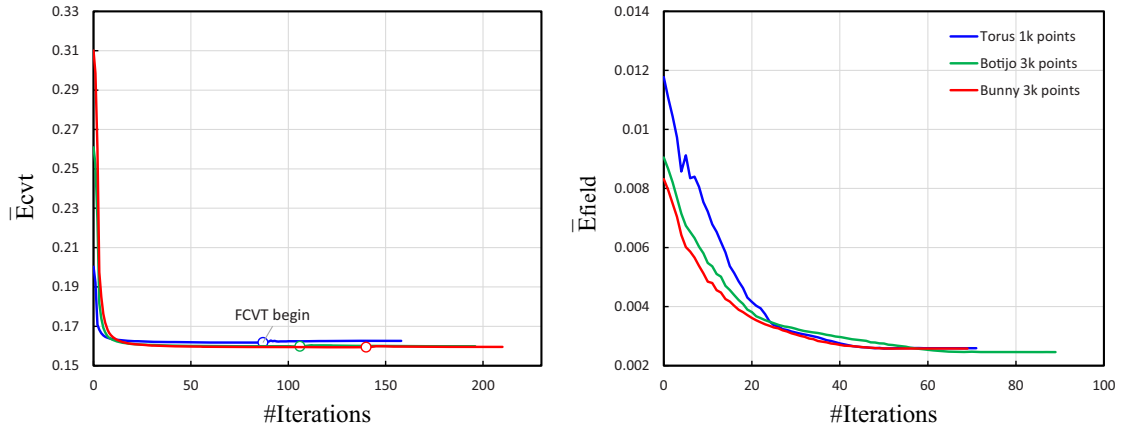
#### 4.4. Valence optimization

After energy optimization, we optimize vertex valence by minimizing the following mesh irregularity energy function:

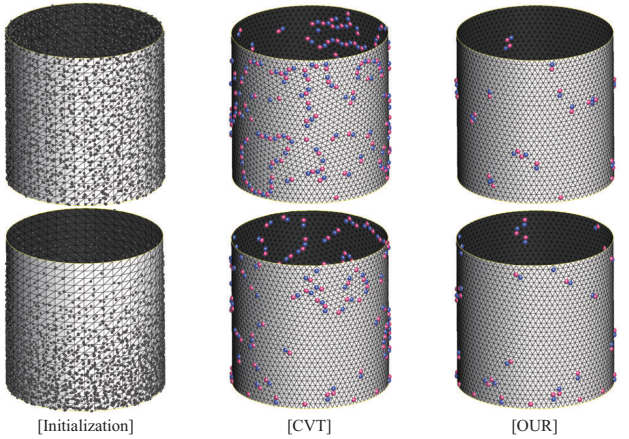
$$R = \sum_{v \in V} (d(v) - o(v))^2,$$



**Figure 7:** Applying proposed approach on cylinder and torus models, whose maximal (top) and minimal (bottom) curvature directions are used as vector field; from left to right of each example: vector fields, and results of IFM, CVT and proposed method.



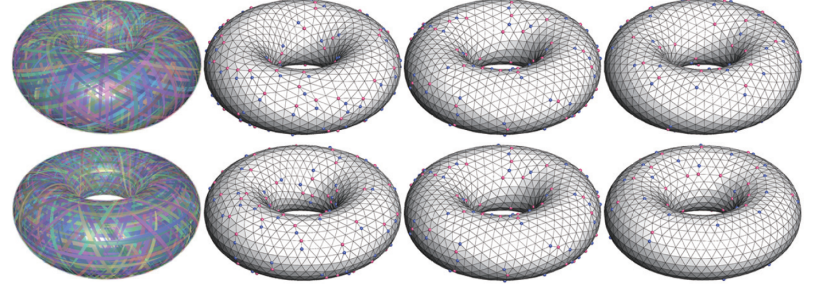
**Figure 8:** Energy analysis; FCVT is performed after pure CVT convergence for three models: Torus (4k faces), Botijo (82k faces) and Bunny (72k faces); FCVT optimization also keeps CVT energy at low level.



**Figure 9:** Influence of uneven initial sampling.

where  $d(v)$  is the valence of  $v$  and  $o(v)$  is the optimal valence of  $v$ , which is usually set as 6 for inner vertices and 4 for boundary vertices.

Similar to previous approaches [BK04, DVBB13], we use three topology operators, that is, edge flip, edge collapse and vertex split,



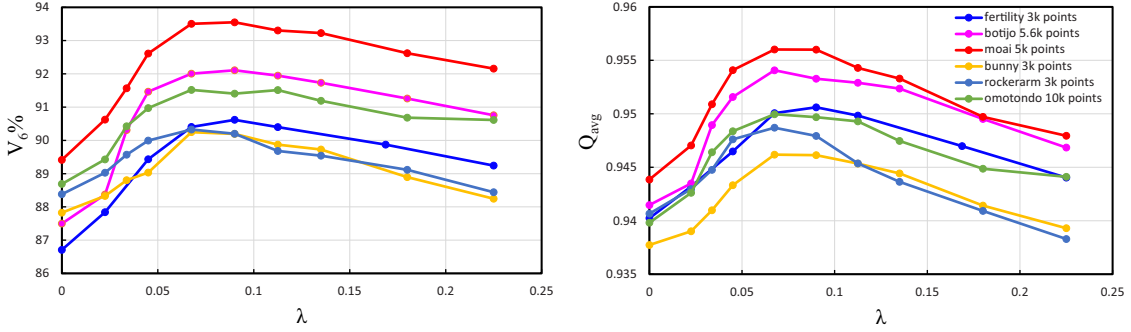
Figure 10: Influence of  $\lambda$ .

Table 1: Influence of valence optimization.

Method	$Q_{avg}$	$\theta_{min}$	$V_6\%$
CVT	0.94	40.3	86.9
CVT_Valence	0.94	39.4	90.7
OUR	0.95	37.8	92.4
OUR_Valence	0.95	37.5	93.7
IFM	0.96	17.7	93.0
IFM_Valence	0.96	19.8	94.5

to minimize the energy function. For each irregular vertex, we find the topology operation that decreases the irregularity energy the most. In each iteration, operations that decrease the irregularity the most are selected and applied. After each topology operation, local tangential smoothing is applied to repair the distortion induced by the operation. After valence optimization, several FCVT iterations are performed to re-align mesh edges from possible deviation caused by valence optimization.

## 5. Experimental Results

We use the open-source library Geogram [geo] for CVT computation and the program Instant Meshes program [JTPS15] for vector field generation. All examples shown in this paper are produced on a PC with 4.00 Ghz CPU, 16 GB RAM and Win10 operating system. To eliminate the influence of the size of input models and the number of target sample points, we set the scale of each input models, thus making the average area per sample point constant. The optimization process is terminated when the  $L_2$  norm of the energy gradient divided by the number of sample points is less than  $10^{-5}$ . The performance and the convergence behaviour of our algorithm are analysed. Then, a detailed analysis of each parameter involved in our method is provided. Finally, we evaluate and compare our results with those of representative state-of-the-art remeshing techniques.

**Convergence and performance.** First, we verify the effectiveness of our algorithm on two specific input models, that is, a cylinder and a torus, whose vector fields are manually chosen to be one of the principal curvature directions. As shown in Figure 7, our

method can capture the field information accurately, even for special inputs. Our results contain very few singular vertices, which cannot be eliminated due to the global nature of mesh connectivity. We compare our results with those of IFM. For the cylinder model, IFM can generate singular-free results because of the open-boundary condition, whereas ours contain a few singularities that can be simply removed by pushing them to the boundary using the singularity move operation proposed in [LZKW10]. For the torus model, our method provides better results with fewer singularities. In both tests, our method exhibits a field alignment property similar to that of IFM and preserves the advantage of good mesh quality of the CVT method (Table 2).

Next, we analyse the convergence behaviour of the proposed energy function. We apply our algorithm to three representative models and observe the convergence behaviour of the CVT energy and field-aligned energy. We track the average energy per sample point during the process. The pure CVT optimization is first applied to acquire a uniform sample distribution. Then, the field alignment term is enforced to improve edge orientation. Figure 8 shows our experimental result. The Torus model has approximately 4k faces and 1k sample points, whereas the Botijo and Bunny models have approximately 80k faces and 3k sample points. Standard CVT and FCVT optimization both converge in approximately 100 iterations. Moreover, the resulting average energy per sample point is nearly constant regardless of input model and number of sample points. These findings verify the stability of our method against various inputs.

Our approach is based on energy minimization; thus, the performance is not as efficient as that of IFM, which is based on vector field tracing. Our algorithm performs slightly poorer in comparison with the standard CVT algorithm [YLL\*09] due to the additional gradient and energy evaluation of the field alignment term. However, the most time-consuming part of the CVT framework is the RVD computation, which has a parallel version of the implementation on multi-core CPUs [geo]; therefore, our algorithm is fast and comparable to other approaches running on a multi-core CPU.

**Uneven initial sampling.** Points are uniformly sampled over the input surface with respect to the density function for initialization. However, our method is also capable of handling uneven



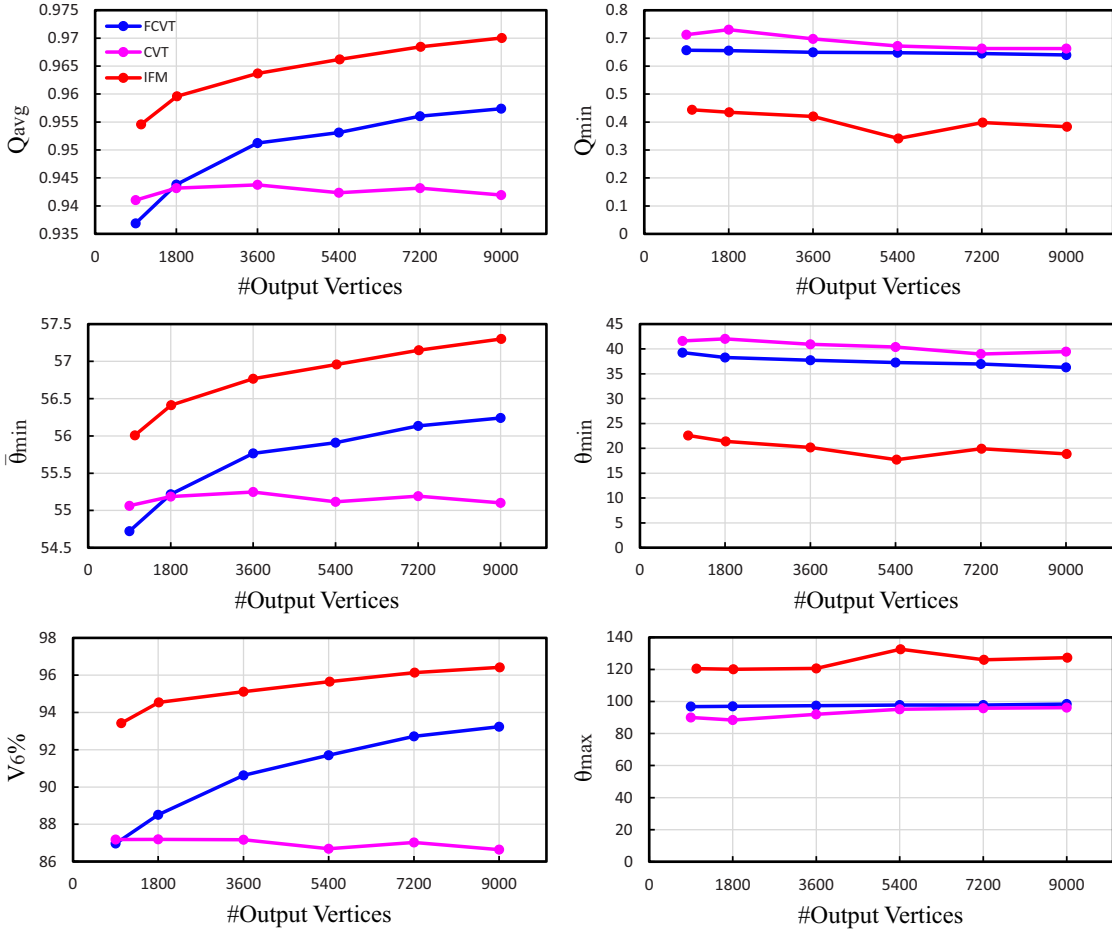


**Figure 11:** Influence of output resolution on mesh quality. The experiment is performed on a torus model with 1.8k vertices. The left column shows FCVT and IFM have improved mesh qualities with denser output resolution. The right column shows that FCVT has preserved the advantage of CVT over IFM on some mesh qualities.

initialization. We first run Lloyd iteration several times to achieve improved initialization, and then switch to the optimization process described in Section 3. We test CVT and our method on a cylinder model with random and uneven initial sampling. Figure 9 shows the results. CVT and our method can properly handle uneven initial sampling.

**Influence of  $\lambda$ .** All the input models are scaled such that the average area per RVC is constant to normalize the parameter  $\lambda$ . We test various choices of  $\lambda$  for different models and resolutions. The overall observation is that a smaller  $\lambda$  results in better triangle quality but more singular vertices and a larger  $\lambda$  reduces the number of singular points but sacrifices mesh quality. Figure 10 shows the influence on valence and average triangle quality of varying  $\lambda$  on different models. For all the experiments, we use a constant  $\lambda$  of 0.0075.

**Valence optimization.** To validate the effectiveness of valence optimization, we compare remeshing results with and without valence optimization on the Botijo model. Three methods (CVT,

FCVT and IFM) are used to remesh the model. Table 1 shows the result. For all methods, the rate of regular vertex increases after valence optimization, thereby affirming the effectiveness of our valence optimization. By contrast, other metrics, such as average quality, are relatively insensitive probably because the regular area already occupies a major part of the mesh before valence optimization, thus making the improvement by valence optimization less remarkable. The experiments also show that FCVT is superior to CVT in average quality and regular rate even without valence optimization.

**Influence of resolution.** We also test the performance of our algorithm under different target mesh resolutions, that is, different numbers of sample points. The experiment is conducted on a torus model with 1.8k vertices. For various target resolutions, we perform CVT, FCVT and IFM and compare the quality of the output meshes. To clarify the comparison, we only focus on the energy minimization stage, and omit valence optimization. For each resolution, the experiment is repeated five times. Figure 11 illustrates the results.

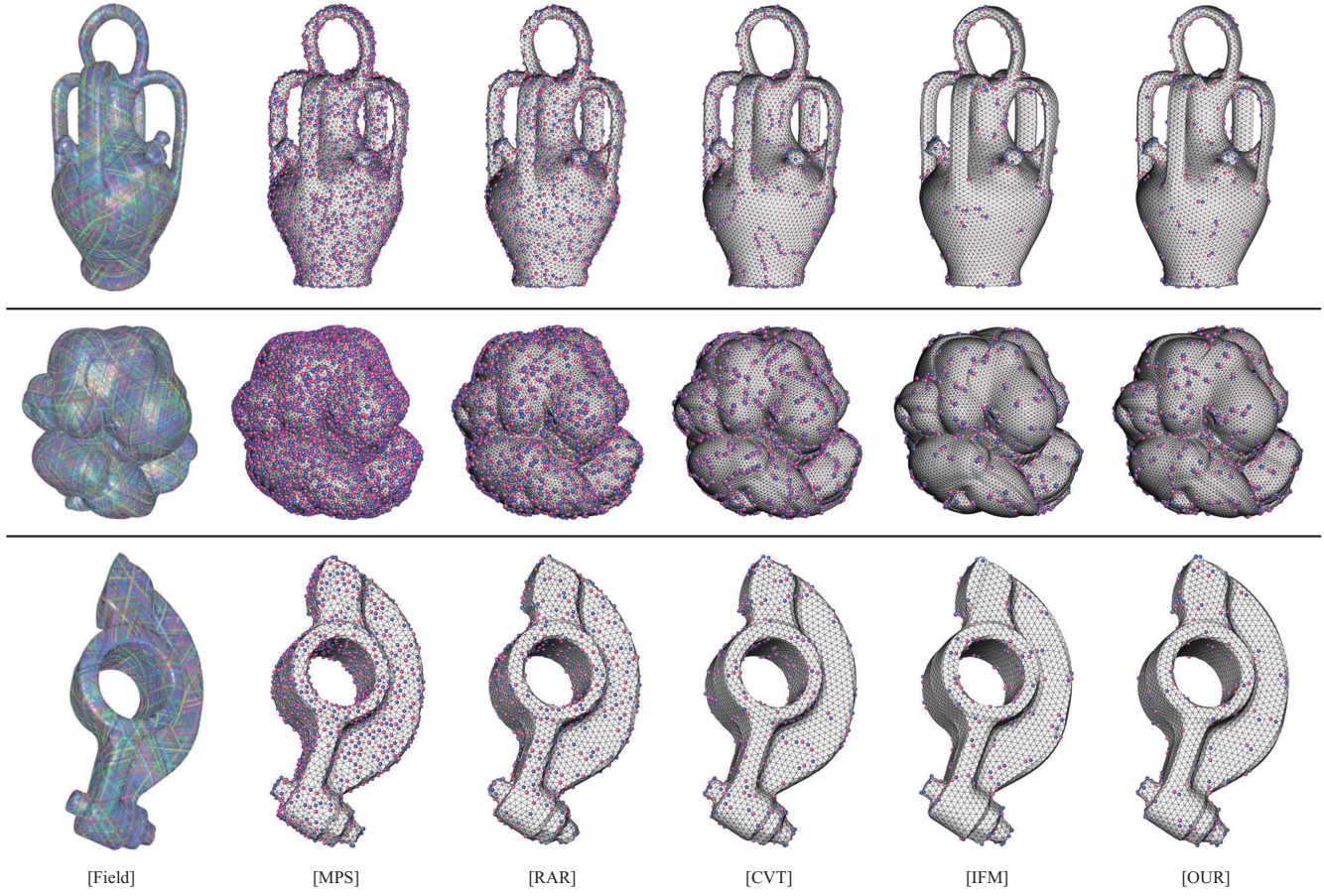


**Figure 12:** Comparison of uniform sampling results; from top to bottom: results of Botijo, Bunny, Omotondo and Rockerarm; from left to right: visualized direction fields and remeshing results of MPS [YW13], RAR [DVBB13], CVT [YLL\*09], IFM [JTPS15] and FFCVT; quality comparison given in Table 2.

We measure two groups of mesh qualities, that is, average and extreme qualities. The average qualities include the average triangle quality  $Q_{avg}$ , average minimal angle  $\bar{\theta}_{min}$  and percentage of valence-6 vertices  $V_6\%$ , which represent mesh quality in an average sense. Extreme qualities, such as  $Q_{min}$ ,  $\theta_{min}$  and  $\theta_{max}$  focus on extreme values and quality bound. In our experiments, the average qualities generally benefit from field alignment, and this effect is further enhanced by increasing the output resolution, as can be seen from the first column of Figure 11. By contrast, extreme qualities are not significantly affected by resolution and deteriorate only slightly with increasing resolution, as illustrated by the second column of Figure 11. Meanwhile, CVT has an evident advantage over IFM in these extreme qualities, which is also preserved by FFCVT.

For extreme mesh qualities, FFCVT inherits the advantage of CVT. In addition, the field alignment capability of FFCVT enables improvement of average qualities and a similar positive response to output resolution, such as IFM. Another interesting observation is that the critical resolution where FFCVT outperforms CVT in average qualities is approximately 1.8k, that is, the resolution of

the input model. This finding is related to the piecewise harmonic field interpolation scheme used by FFCVT. The piecewise harmonic interpolation may lead to a smoother field in the interior of a triangle than at the common edge of two adjacent triangles. With increasing resolution, more pairs of adjacent sample points share the same input triangle rather than reside on different triangles, thus improving overall energy smoothness and improving mesh quality. The results in the left column of Figure 11 also validate the effectiveness of our field interpolation algorithm. According to [JTPS15], IFM requires the input mesh to have higher resolution than the output; otherwise, the input mesh has to be further subdivided. These results imply that our interpolated field is comparable with the field produced by the ‘subdivide and optimize’ process of IFM.

**Sharp feature handling.** Our method is also able to handle input meshes with sharp features. The features on the input mesh are either detected automatically by certain algorithms or manually selected by the user. Similar to [YLL\*09], a two-stage strategy is used to preserve sharp features. In the first stage, sample points are optimized freely to obtain an optimal distribution. In the second

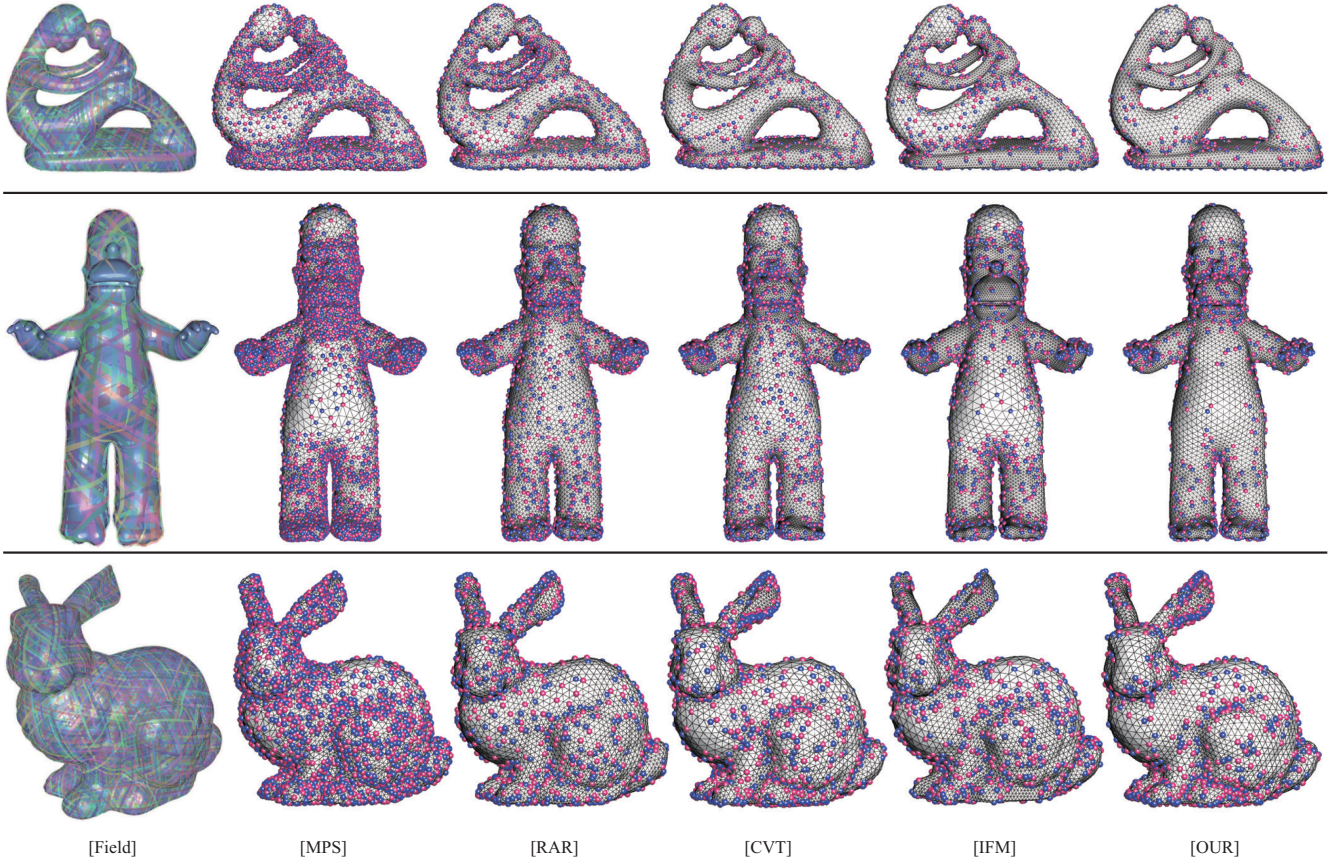


**Figure 13:** Comparison of adaptive sampling results; From left to right: visualized of direction fields, remeshing results of MPS [YW13], RAR [DVBB13], CVT [YLL\*09], IFM [JTPS15] and ours. The quality comparison given in Table 2.

stage, each sample point whose RVC intersects with a feature line is snapped onto the line and confined on the feature in the following optimization. Figure 14 shows several results of our method applied to models with sharp features.

**Comparison.** We first compare our approach with the most related approaches, that is, CVT and IFM, in terms of visual effect and mesh quality. Our results are obtained by first applying 65 CVT iterations and then 65 FCVT iterations. The results of CVT are obtained by applying 130 CVT iterations (or less if converged earlier). The visual effect (Figures 1, 7, 12 and 13) shows that our results are well aligned to the underlying vector fields, which are able to capture the anisotropic features as well as produce well-shaped triangle. Moreover, the singular point distribution of our approach is similar to that of IFM.

We compare our method with IFM [JTPS15] on adaptive remeshing in Figure 13. Adapting the edge length locally is difficult due to the global nature of IFM, thereby resulting in a large distortion in regions with highly changing density. Figure 15 shows another example that uses a density function with large gradation.

Our results are compared with several representative state-of-the-art approaches, including *maximal Poisson-disk sampling*

(MPS) [YW13], *realtime adaptive remeshing* (RAR) based on local connectivity optimization [DVBB13]. We use the standard mesh quality evaluation metric for comparison. The quality of a triangle is measured by  $Q(t) = \frac{2\sqrt{3}|t|}{p_t h_t}$ , where  $|t|$  is the area of triangle  $t$ ,  $p_t$  the inscribed radius of  $t$  and  $h_t$  the length of the longest edge of  $t$ . An equilateral triangle has  $Q(t) = 1$  and a degenerate triangle has  $Q(t) = 0$  [FB97]. Table 2 lists the numerical statistics of all the compared approaches. In addition to the quality measured in Figure 11, we count the percentage of the triangles with small and large angles, for example,  $\theta_{min} < 30^\circ$  and  $\theta_{max} > 90^\circ$ , which reflect the overall triangle quality distribution of each method. Finally, we measure the Hausdorff distance and the root mean square error between the remesh and the input mesh. From quantitative comparison, our approach preserves the advantages of isotropic and field remeshing. For most models in the experiments, our results have better  $\theta_{min}$  than IFM, and better regularity than MPS, RAR and CVT.

**Limitation.** Our current approach has certain limitations. First, in the adaptive sampling scenario, the remeshing result is not as good as that of CVT, because the density function always conflicts with the field alignment constraint. Another limitation is that the field interpolation is somehow time consuming; in this process, we have to project each sample back onto the surface and transverse

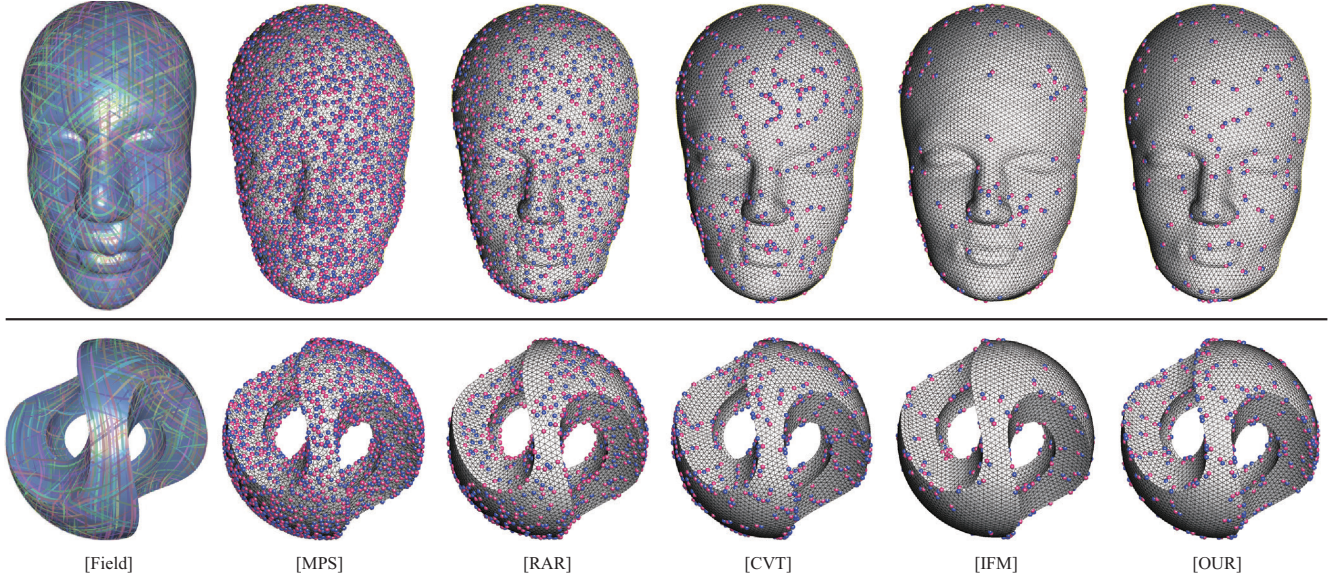


**Figure 14:** Results of feature preservation.

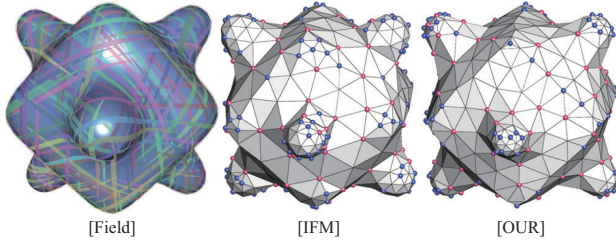


**Figure 15:** Comparison of adaptive remeshing with IFM. Both IFM and our method are able to generate meshes with large triangle area contrast. However, our result better aligns to the underlying shape and is less distorted compared to the result of IFM.

all combinations of representative vectors. We plan to address upon these problems in our future work.

## 6. Conclusion and Future Work

We present a novel approach that combines the CVT-based isotropic remeshing with vector field alignment. Unlike approaches that modify the distance metrics [LL10, SCW\*11], we impose the field alignment as a penalty term added to the standard CVT energy function, thus simplifying implementation. Our results exhibit the advantages of isotropic and field-aligned remeshing, that is, few singularities and high mesh quality. In the future, we plan to use the field defined on facets instead of vertices, which may improve performance. Another interesting problem is finding the correspondence between singularities of the input field and resulting mesh, which may help to detect and eliminate unnecessary singular vertices. Reducing the shape approximation error is also of considerable interest. We would also like to further exploit the power of our approach in potential applications.

## Acknowledgements

We are grateful to anonymous reviewers for their suggestive comments. We would like to thank Wenzel Jacob and Daniele Panozzo for sharing the source code of the adaptive version of IFM [JTPS15] for comparison. This work is partially funded by the National Natural Science Foundation of China (61373070, 61772523, 61372168, 61379096, 61620106003).

## Appendix: Partial Derivatives of Field Alignment Energy

In this Appendix, we derive the closed-form partial derivatives of the field alignment energy function, which is required by quasi-Newton optimization methods. Since 2D planar mesh can be regarded as a special case of surface mesh, we focus on the field alignment energy of 3D surface mesh.

Given a sample point  $\mathbf{x}_i$  and its neighbour point  $\mathbf{x}_j$ , and the edge  $e$  connecting these two points. The contribution of edge  $e$  to the total field alignment energy comes from its two opposite directions  $\mathbf{e}_{ij} = \mathbf{x}_j - \mathbf{x}_i$  and  $\mathbf{e}_{ji} = -\mathbf{e}_{ij}$ ,

$$\begin{aligned} E_e &= E_{ij} + E_{ji} \\ &= w_{ij} \cdot D_{ij} + w_{ji} \cdot D_{ji} \\ &= w_{ij} \cdot D(\mathbf{e}_{ij}, \mathbf{n}_i, \mathbf{d}_i) + w_{ji} \cdot D(\mathbf{e}_{ji}, \mathbf{n}_j, \mathbf{d}_j), \end{aligned}$$

where  $w_{ij}$  and  $w_{ji}$  are edge weights,  $\mathbf{n}_i, \mathbf{n}_j, \mathbf{d}_i, \mathbf{d}_j$  are normal and field vectors at the two points, and  $D$  is the direction distance function.

Viewing the edge weights as a constant, the partial derivative of  $E_e$  with respect to point  $\mathbf{x}_i$  is

$$\frac{\partial E_e}{\partial \mathbf{x}_i} = w_{ij} \frac{\partial D(\mathbf{e}_{ij}, \mathbf{n}_i, \mathbf{d}_i)}{\partial \mathbf{x}_i} + w_{ji} \frac{\partial D(\mathbf{e}_{ji}, \mathbf{n}_j, \mathbf{d}_j)}{\partial \mathbf{x}_i}.$$



- [AGY\*17] AHMED A., GUO J., YAN D.-M., FRANCESCHI J.-Y., ZHANG X., DEUSSEN O.: A simple push-pull algorithm for blue-noise sampling. *IEEE Transactions on Visualization and Computer Graphics* 23, 12 (2017), 2496–2508.
- [AMD02] ALLIEZ P., MEYER M., DESBRUN M.: Interactive Geometry Remeshing. *ACM Transactions on Graphics (Proc. SIGGRAPH)* 21(3) (2002), 347–354.
- [AUGA08] ALLIEZ P., UCELLI G., GOTSMAN C., ATTENE M.: Recent advances in remeshing of surfaces. In *Shape Analysis and Structuring*, L. De Floriani and M. Spagnuolo (Eds.), Springer, Heidelberg (2008), pp. 53–82.
- [AVDI03] ALLIEZ P., VERDIÉRE É. C. D., DEVILLERS O., ISENBURG M.: Isotropic surface remeshing. In *Proceedings of Shape Modeling International—SMI* (2003), M. S. Kim (Ed.), IEEE Computer Society, Los Alamitos, pp. 49–58.
- [AYZ12] AGHDAAI N., YOUNES H., ZHANG H.: 5–6–7 meshes: Remeshing and analysis. *Computers & Graphics* 36, 8 (2012), 1072–1083.
- [BK04] BOTSCHE M., KOBELT L.: A remeshing approach to multiresolution modeling. In *Proceedings of Symposium of Geometry Processing* (Nice, France, 2004), R. Scopigno and D. Zorin (Eds.), ACM, New York, NY, USA, pp. 189–196.
- [BKP\*10] BOTSCHE M., KOBELT L., PAULY M., ALLIEZ P., LÉVY B.: *Polygon Mesh Processing*. AK Peters, Natick, Massachusetts, Boca Raton, FL, 2010.
- [BLP\*13] BOMMES D., LÉVY B., PIETRONI N., PUPPO E., SILVA C. T., TARINI M., ZORIN D.: Quad-mesh generation and processing: A survey. *Computer Graphics Forum* 32, 6 (2013), 51–76.
- [BLW10] BRONSON J. R., LEVINE J. A., WHITAKER R. T.: Particle systems for adaptive, isotropic meshing of CAD models. In *Proceedings of the 19th International Meshing Roundtable* (2010), S. Shontz (Ed.), Springer, Berlin, Heidelberg, pp. 279–296.
- [Boi05] BOISSONNAT J.-D. O. S.: Provably good sampling and meshing of surfaces. *Graphical Models* 67 (2005), 405–451.
- [BSTY15] BOISSONNAT J., SHI K., TOURNOIS J., YVINEC M.: Anisotropic Delaunay meshes of surfaces. *ACM Transactions on Graphics* 34, 2 (2015), 14:1–14:11.
- [CCW12] CHEN Z., CAO J., WANG W.: Isotropic surface remeshing using constrained centroidal Delaunay mesh. *Computer Graphics Forum* 31, 7-1 (2012), 2077–2085.
- [CDS12] CHENG S.-W., DEY T. K., SHEWCHUK J. R.: *Delaunay Mesh Generation*. CRC Press, Boca Raton, FL, 2012.
- [Che93] CHEW L. P.: Guaranteed-quality mesh generation for curved surfaces. In *Proceedings of the Ninth Symposium on Computational Geometry* (San Diego, California, USA, 1993), ACM, New York, NY, USA, pp. 274–280.
- [Che04] CHEN L.: Mesh smoothing schemes based on optimal Delaunay triangulations. In *Proceedings of 13th International Meshing Roundtable* (2004), pp. 109–120.
- [DFG99] DU Q., FABER V., GUNZBURGER M.: Centroidal Voronoi tessellations: Applications and algorithms. *SIAM Review* 41 (1999), 637–676.
- [dGDT16] DE GOES F., DESBRUN M., TONG Y.: Vector field processing on triangle meshes. In *SIGGRAPH ’16: ACM SIGGRAPH 2016 Courses* (New York, NY, USA, 2016), ACM, pp. 27:1–27:49.
- [DKG05] DONG S., KIRCHER S., GARLAND M.: Harmonic functions for quadrilateral remeshing of arbitrary manifolds. *Computer Aided Geometric Design* 22, 5 (2005), 392–423.
- [DVBB13] DUNYACH M., VANDERHAEGHE D., BARTHE L., BOTSCHE M.: Adaptive remeshing for real-time mesh deformation. In *Eurographics Short Papers Proceedings* (2013), The Eurographics Association, pp. 29–32.
- [ERA\*16] EBIDA M., RUSHDI A. A., AWAD M. A., MAHMOUD A. H., YAN D.-M., ENGLISH S. A., OWENS J. D., BAJAJ C. L., MITCHELL S. A.: Disk density tuning of a maximal random packing. *Computer Graphics Forum (Proc. SGP)* 35, 5 (2016), 259–269.
- [FAKG10] FUHRMANN S., ACKERMANN J., KALBE T., GOESELE M.: Direct resampling for isotropic surface remeshing. In *Proceedings of the Vision, Modeling, and Visualization Workshop 2010* (2010), R. Koch, A. Kolb and C. Rezk-Salama (Eds.), The Eurographics Association, pp. 9–16.
- [FB97] FREY P. J., BOROUCHAKI H.: Surface mesh evaluation. In *IMR* (1997), pp. 363–374.
- [FLSG14] FU X., LIU Y., SNYDER J., GUO B.: Anisotropic simplicial meshing using local convex functions. *ACM Transactions on Graphics (Proc. SIGGRAPH Asia)* 33, 6 (2014), 182:1–182:11.
- [FZ08] FU Y., ZHOU B.: Direct sampling on surfaces for high quality remeshing. In *ACM Symposium on Solid and Physical Modeling* (2008), pp. 115–124.
- [geo] GEOGRAM. <https://gforge.inria.fr/projects/geogram/> (accessed February 23, 2018).
- [GYJZ15] GUO J., YAN D.-M., JIA X., ZHANG X.: Efficient maximal Poisson-disk sampling and remeshing on surfaces. *Computers & Graphics* 46, 6-8 (2015), 72–79.
- [HDD\*93] HOPPE H., DEROSSE T., DUCHAMP T., McDONALD J., STUETZLE W.: Mesh optimization. In *Proceedings of ACM SIGGRAPH* (New York, NY, USA, 1993), ACM, pp. 19–26.
- [HJ16] HUANG Z., JU T.: Extrinsic smooth direction fields. *Computers & Graphics* 58 (2016), 109–117.
- [HYB\*17] HU K., YAN D.-M., BOMMES D., ALLIEZ P., BENES B.: Error-bounded and feature preserving surface remeshing with minimal angle improvement. *IEEE Transactions on Visualization and Computer Graphics* 23, 12 (2017), 2560–2573.
- [HZP\*11] HUANG J., ZHANG M., PEI W., HUA W., BAO H.: Controllable highly regular triangulation. *SCIENCE CHINA Information Sciences* 54, 6 (2011), 1172–1183.

- [JTPS15] JAKOB W., TARINI M., PANZOZZO D., SORKINE-HORNUNG O.: Instant field-aligned meshes. *ACM Transactions on Graphics (Proc. SIGGRAPH Asia)* 34, 6 (2015), 189:1–189:15.
- [LB12] LÉVY B., BONNEEL N.: Variational anisotropic surface meshing with Voronoi parallel linear enumeration. In *Proceedings of the 21st International Meshing Roundtable* (2012), Springer, Berlin, Heidelberg, pp. 349–366.
- [LJX\*10] LAI Y., JIN M., XIE X., HE Y., PALACIOS J., ZHANG E., HU S., GU X.: Metric-driven RoSy field design and remeshing. *IEEE Transactions on Visualization and Computer Graphics* 16, 1 (2010), 95–108.
- [LL10] LÉVY B., LIU Y.:  $L_p$  centroidal Voronoi tessellation and its applications. *ACM Transactions on Graphics (Proc. SIGGRAPH)* 29, 4 (2010), 119:1–11.
- [LWH\*15] LEUNG Y., WANG X., HE Y., LIU Y., WANG C. C. L.: A unified framework for isotropic meshing based on narrow-band Euclidean distance transformation. *Computational Visual Media* 1, 3 (2015), 239–251.
- [LWL\*09] LIU Y., WANG W., LÉVY B., SUN F., YAN D.-M., LU L., YANG C.: On centroidal Voronoi tessellation: Energy smoothness and fast computation. *ACM Transactions on Graphics* 28, 4 (2009), 101:1–101:11.
- [LXW\*11] LIU Y., XU W., WANG J., ZHU L., GUO B., CHEN F., WANG G.: General planar quadrilateral mesh design using conjugate direction field. *ACM Transactions on Graphics (Proc. SIGGRAPH Asia)* 30, 6 (2011), 140:1–140:10.
- [LXY\*16] LIU Y.-J., XU C.-X., YI R., FAN D., HE Y.: Manifold differential evolution (MDE): A global optimization method for geodesic centroidal Voronoi tessellations on meshes. *ACM Transactions on Graphics (Proc. SIGGRAPH Asia)* 35, 6 (2016), 243:1–11.
- [LZKW10] LI Y., ZHANG E., KOBAYASHI Y., WONKA P.: Editing operations for irregular vertices in triangle meshes. *ACM Transactions on Graphics (Proc. SIGGRAPH Asia)* 29, 6 (2010), 153:1–153:11.
- [MKW07] MEYER M., KIRBY R., WHITAKER R.: Topology, accuracy, and quality of isosurface meshes using dynamic particles. *IEEE Transactions on Visualization and Computer Graphics* 13, 6 (2007), 1704C1711.
- [NPPZ11] NIESER M., PALACIOS J., POLTHIER K., ZHANG E.: Hexagonal global parameterization of arbitrary surfaces. *IEEE Transactions on Visualization and Computer Graphics* 18, 6 (2011), 865–878.
- [Ren16] RENKA R. J.: Two simple methods for improving a triangle mesh surface. *Computer Graphics Forum* 35, 6 (2016), 46–58.
- [SAG03] SURAZHSKY V., ALLIEZ P., GOTSMAN C.: Isotropic remeshing of surfaces: A local parameterization approach. In *In 12th International Meshing Roundtable* (2003), pp. 204–231.
- [SCW\*11] SUN F., CHOI Y.-K., WANG W., YAN D.-M., LIU Y., LÉVY B.: Obtuse triangle suppression in anisotropic meshes. *Computer Aided Geometric Design* 28, 9 (2011), 537–548.
- [SSG03] SIFRI O., SHEFFER A., GOTSMAN C.: Geodesic-based surface remeshing. In *Proceedings of the 12th International Meshing Roundtable, IMR 2003* (2003), Kluwer Academic Publishers, pp. 189–199.
- [Tur92] TURK G.: Re-tiling polygonal surfaces. In *Proceedings of ACM SIGGRAPH* (New York, NY, USA, 1992), ACM, pp. 55–64.
- [VCD\*16] VAXMAN A., CAMPEN M., DIAMANTI O., BOMMES D., HILDEBRANDT K., BEN-CHEN M., PANZOZZO D.: Directional field synthesis, design, and processing. In *SA '16 SIGGRAPH ASIA 2016 Courses* (New York, NY, USA, 2016), ACM, pp. 15:1–15:30.
- [VCP08] VALETTE S., CHASSERY J.-M., PROST R.: Generic remeshing of 3D triangular meshes with metric-dependent discrete Voronoi diagrams. *IEEE Transactions on Visualization and Computer Graphics* 14, 2 (2008), 369–381.
- [WYL\*15] WANG X., YING X., LIU Y.-J., XIN S.-Q., WANG W., GU X., MUELLER-WITTIG W., HE Y.: Intrinsic computation of centroidal Voronoi tessellation (CVT) on meshes. *Computer-Aided Design* 58 (2015), 51–61.
- [YBZW14] YAN D.-M., BAO G., ZHANG X., WONKA P.: Low-resolution remeshing using the localized restricted Voronoi diagram. *IEEE Transactions on Visualization and Computer Graphics* 20, 10 (2014), 418–427.
- [YLL\*09] YAN D.-M., LÉVY B., LIU Y., SUN F., WANG W.: Isotropic remeshing with fast and exact computation of restricted Voronoi diagram. *Computer Graphics Forum (Proc. SGP)* 28, 5 (2009), 1445–1454.
- [YW13] YAN D.-M., WONKA P.: Gap processing for adaptive maximal Poisson-disk sampling. *ACM Transactions on Graphics* 32, 5 (2013), 148:1–148:15.
- [YW16] YAN D., WONKA P.: Non-obtuse remeshing with centroidal Voronoi tessellation. *IEEE Transactions on Visualization and Computer Graphics* 22, 9 (2016), 2136–2144.
- [ZGW\*13] ZHONG Z., GUO X., WANG W., LÉVY B., SUN F., LIU Y., MAO W.: Particle-based anisotropic surface meshing. *ACM Transactions on Graphics (Proc. SIGGRAPH)* 32, 4 (2013), 99:1–99:14.
- [Zha16] ZHANG E.: Course notes rotational symmetries on surfaces: Theory, algorithms, and applications. In *SA '16 SIGGRAPH ASIA 2016 Courses* (New York, NY, USA, 2016), ACM, pp. 10:1–10:13.